Analysis and design of dispersion-engineered cascaded channel waveguide for mid-infrared supercontinuum generation employing pump source at telecommunication wavelength

M. R. Karim[a,*], Nayem Al Kayed[b], B. M. A. Rahman[c]

[a]*Department of Electrical and Electronic Engineering, Chittagong Independent University, Chittagong, Bangladesh*
[b]*Department of Electrical and Electronic Engineering, Chittagong University of Engineering and Technology, Chittagong, Bangladesh*
[c]*Department of Electrical and Electronic Engineering, City University of London, Northampton Square, London, EC1V 0HB, UK*

Abstract

We theoretically investigate and propose a promising 8-mm-long cascade planar waveguide made of Si_3N_4 and As_2Se_3 glass system for mid-infrared supercontinuum generation by employing a commercially available femtosecond pump source operating at 1550 nm wavelength. A rigorous numerical investigation has been performed considering three different dispersion regions of the optimized cascade waveguide for expanding the SC coverage far into the mid-infrared. Based on the tailored dispersion region whether the anomalous or normal, the pump pulse is applied at the input of the initial waveguide segment of Si_3N_4 and the output of which is then coupled into the final waveguide segment made of As_2Se_3 glass system. The output supercontinuum spectrum for all-anomalous dispersion region expanded up to 10 μm by one of the best reported so far using cascade design with coherency of unity over the entire spectrum region predicted. This would be the widest spectral coverage expanded into the mid-infrared, to the best of the authors' knowledge, by the cascade planar waveguide design employing a commercially available pump source in telecommunication window with a peak power of 5 kW. Such a highly coherent cascade planar waveguide, designed and proposed based on the concatenating principle for a broadband mid-infrared supercontinuum generation using the two-step process, would be highly suitable for many mid-infrared based applications such as sensing and biological imaging.

Keywords: Cascade planar waveguide, Nonlinear optics, Dispersion, Chalcogenide, Supercontinuum generation

1. Introduction

Broadband supercontinuum (SC) sources made using chalcogenide glass systems are the promising candidate for mid-infrared (MIR) sensing, imaging, and spectroscopic applications [1]. To be particular, generation of SC in the MIR has drawn attention as this wavelength region offers strong absorption bands for organic compounds such as sugars, proteins, lipids which can be useful for separation of malignant from benign tissue in regard of skin cancer investigation [2, 3]. The design of SC light sources, in detecting air pollution [4] and tracing hazardous components [5] through atmospheric molecules absorption bands in the MIR spectrum range, have grown interest among the researchers in recent years. To date, an intense amount of research has concentrated on spanning the wavelength over MIR in the range 2–20 μm as the molecular fingerprint region has fallen in this range which covers up the various crucial MIR applications [6, 7, 8, 9, 10, 11, 12, 13, 14, 15, 16].

In recent decades, exploration of the SC generation theoretically and experimentally were performed in the MIR through different kinds of highly nonlinear materials: chalcogenides (ChG) [10, 11] and tellurides [17, 18] glass systems. The efficient SC generation in the MIR have successfully demonstrated up to 14 μm by ChG [10] and 15 μm by telluride material [18] based fiber systems. Technological development in optics has given the researchers a platform with the freedom to focus the SC spanning in different types of optical systems such as integrated waveguides and optical fiber system. Fiber systems have design flexibility, easy control on the nonlinearity and dispersion. However, long length fiber based design have incurred high propagation losses during SC generation. To address this problem, short length low cost planar waveguides can be a promising candidate as a counterpart in the SC source design. Modern well developed integrated waveguides fabrication facilities have accelerated the MIR SC generation in the integrated photonics platforms [19, 20, 21, 22, 23, 24].

It is important to know that an effective effort to realize the MIR SC experimentally and theoretically by tuning the center wavelength of the femtosecond pump source in the MIR [24, 25]. However, such pump sources are not widely available for commercial purposes due to higher cost and complexity [26]. The pump source with wavelength range between 2.5–4.1 μm and peak power of 1–10

---

kW are potential candidates because of commercial feasibility [27, 28, 29]. However, they are confined in academic interest due to unavailability as commercial products. Thus, to address these issues, new approaches for expanding the MIR SC with commercially available short wavelength pump sources are baldly required. Cascading two optimized waveguide segments using the easiest experimental setup to implement in practice with the aid of commercially available pump sources can be a good choice [30]. The cascade system creates the opportunity to use readily available pump source at the telecommunication band. Through step-wise extension toward the MIR due to progressively red-shifting of initial pulse in the cascade system is performed. The main key idea behind the extension of MIR SC through cascading dispersion-engineered highly nonlinear waveguides is that the propagated pulse strongly enhances the soliton self-frequency shift (SSFS) while it progressively propagated inside the cascaded waveguides [31].

Several research groups successfully demonstrated the MIR SC generation through optical fiber based cascaded system employing pump source relatively to shorter wavelength regions in the telecommunication window [26, 32, 33, 34, 35, 36, 31]. Kubat *et al.* [26] realized the SC spectrum spanning up to 7 μm by concatenating a ZBLAN fiber with the ChG fiber by utilizing a 2 μm Tm fiber laser source. Tang *et al.* [32] demonstrated concatenating photonic crystal fiber (PCF) with fluoride fiber to obtained spectral coverage of 2–4.3 μm. Doped and undoped ZBLAN fiber with ChG fiber concatenating for SC expansion up to 8 μm was reported by Robichaud *et al.* [33]. Highly coherent SC generation from 0.78 to 8.3 μm using a pump at 2 μm wavelength through two-step SC (2S-SC) by cascading tellurite and ChG fibers was numerically demonstrated by Nguyen *et al.* [34]. Theberge *et al.* [35] reported an MIR SC coverage between 1.4 μm and 6.4 μm using a concatenated step-index InF$_3$ and As$_2$Se$_3$ fibers pumped by an all-fiber laser source. Peterson *et al.* [36] demonstrated the MIR SC up to 7 μm using cascaded silica-fluoride-ChG fiber. The experimental demonstration of cascaded silica-ZBLAN-ChG fibers system using commercially available components was reported by Venck *et al.* [31] and they have demonstrated the SC spanning in the range 2–10 μm by using commercially available pump source at 1.55 μm. There is no doubt regards on the successful demonstration of the SC generation in the fiber based system by cascading approaches described above. However, the cascading approaches employing in integrated planar waveguide system is still unexplored. The realization of this issue has motivated us to carry out the rigorous study on MIR SC generation at the output of cascade waveguide by considering the various combination of dispersion regions as anomalous to anomalous, anomalous to normal or all-normal dispersion pulse propagation inside the waveguide structure employing pump at telecommunication wavelength.

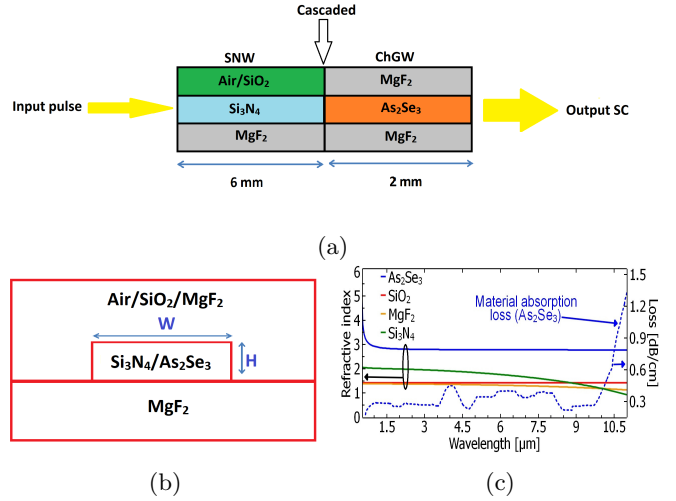In this study, we have proposed a 8-mm-long cascade

Figure 1: Schematics and refractive index profile for 2S-SC generation: (a) Proposed cascade waveguide system consists of SNW and ChGW; (b) Transverse dimensional view of the proposed waveguide; and (c) Refractive index profiles and propagation (absorption) loss plots for the materials used.

waveguide made of two independent waveguide sections for 2S-SC generation in the MIR. Spectral coverage at the output of cascade waveguide is investigated for three different GVD regions: 1) All-anomalous dispersion region SC generation; 2) Normal to anomalous GVD region SC generation; and 3) All-normal dispersion SC generation. At the output of cascade waveguide optimized using the three GVD regions mentioned above, MIR SC spectral coverage from 0.86 to 10 μm can be obtained with a commercially available telecom wavelength pump source at 1550 nm and peak power of 5 kW. To the best of the authors' knowledge, this would be the widest MIR spectral coverage predicted using the cascade planar waveguide proposed by using commercially available pump source employed at 1550 nm wavelength. Finally, the effect of power variations and the degree of spectral coherence at the output of proposed cascade waveguide have been performed and discussed.

2. Theoretical Model

The proposed waveguide setup for 2S-SC generation is demonstrated in Fig. 1(a). Here two optimized dispersion-engineered rectangular channel waveguides are concatenated. The core of first waveguide segment (SNW) where the input pulse from pump source applied is made of Si$_3$N$_4$ and the core of second waveguide segment (ChGW) is made with As$_2$Se$_3$ glass material. During carrying out simulations, two separate initial SNW segments are considered: one is made of air–Si$_3$N$_4$ (Air–SNW, upper-cladding and core) and other is made of SiO$_2$–Si$_3$N$_4$ (Silica–SNW, upper-cladding and core). MgF$_2$ is chosen for upper cladding of 2nd waveguide segment and lower claddings of both of the waveguide segments proposed. To achieve minimum coupling loss during cascading, same material is used as

Table 1: **Material properties considered during simulation of 2S-SC generation**

Material Properties	As_2Se_3 [37, 38]	Si_3N_4 [39, 40]
Kerr-index (n_2) [m^2/W]	1.1×10^{-17}	2.5×10^{-19}
Material Propagation Loss [dB/cm]	0.65	0.7
Transmission Limit [μm]	0.85–17.5	0.4–4.6
f_R	0.148	–
τ_1 [fs]	23	–
τ_2 [fs]	164.5	–

bottom cladding for both of the waveguide segments. The vision of this work is to analyze pulse propagation inside the cascade structure in different dispersion region rigorously. Initial waveguide, SNW is optimized by considering its transverse dimensional parameters width (W) and thickness (H) for pumping it either of anomalous or normal GVD region separately. Similar approach is employed for optimizing the final segment of the waveguide, ChGW. The waveguide transverse cross-section indicating core and cladding materials is illustrated in Fig. 1(b).

To perform the linear analysis of a cascade structure, the required refractive index of proposed materials up to the interesting wavelength region are calculated from [23, 41, 42, 43]. The refractive index plots corresponding to the materials proposed: Si_3N_4, SiO_2, As_2Se_3, and MgF_2 are illustrated in Fig. 1(c). The propagation loss edge [44] considered for the As_2Se_3 glass system is also illustrated in Fig. 1(c) and the absorption loss for this glass system is reported 0.65 dB/cm at 10.6 μm by Shiryaev *et al.* [37]. The required optical properties at 1.55 μm wavelength for generating efficient SC in the MIR are mentioned in Table 1. The optical transparency of MgF_2 material beyond 7 μm is reported by Duchesne *et al.* [45]. The cascade structure, which is a concatenated form of SNW and ChGW, has been optimized through finite-element based COMSOL Multiphysics. COMSOL provides the effective refractive index (n_{eff}) and mode effective area (A_{eff}) of the fundamental quasi-transverse electric (FQTE, H_y^{11}) mode for the proposed structure up to the interested wavelength region, which is later used to compute the most significant parameters: group-velocity dispersion (GVD, D) and nonlinear co-efficient (γ) [46] [47].

The mode field mismatch at the junction point between the two segments of the cascade waveguide structure can be calculated using the overlap integral (OI) [47] as follows:

$$OI = \frac{(\iint H_{1y}.H_{2y} \; dxdy)}{\sqrt{(\iint H_{1y}^2 dxdy).(\iint H_{2y}^2 dxdy)}} \quad (1)$$

where H_{1y} and H_{2y} are the mode field distribution of the fundamental mode of the initial and final segments of the cascade design, respectively.

To observe the 2S-SC evolution inside the cascade waveguide proposed, the generalized nonlinear Schrödinger equation (GNLSE) for the fundamental mode is employed as

follows [46]:

$$\frac{\partial}{\partial z}A(z,T) = -\frac{\alpha}{2}A + \sum_{k \geq 2}^{12} \frac{i^{k+1}}{k!} \beta_k \frac{\partial^k A}{\partial T^k} + i\gamma \left(1 + \frac{i}{\omega_0}\frac{\partial}{\partial T}\right)$$
$$\times \left(A(z,T) \int_{-\infty}^{\infty} R(T) \mid A(z,T-T') \mid^2 dT' \right),$$
$$(2)$$

where $A(z,T)$ is expressed as the complex amplitude of time-domain pulse envelop; z and T are, respectively, the propagation distance and the time related to the group-velocity at the center frequency (ω_0) of optical pulse; γ is the nonlinear co-efficients of the proposed cascade waveguide; β_k is the kth order GVD coefficient calculated for the cascade waveguide at the ω_0; and $R(T)$ is the nonlinear (Raman) response of the material considered for our proposed design, which is given by [30, 46]:

$$R(t) = (1 - f_R)\delta(t) + f_R h_R(t), \quad (3)$$

which includes the Kerr component and the Raman contribution having the form

$$h_R(t) = \frac{\tau_1^2 + \tau_2^2}{\tau_1 \tau_2^2} \exp\left(-\frac{t}{\tau_2}\right) \sin\left(\frac{t}{\tau_1}\right), \quad (4)$$

where the values of f_R, τ_1 and τ_2 corresponding to the material proposed are mentioned in Table 1.

The GNLSE is solved by our in-house developed MATLAB code following split-step Fourier method (SSFM) [21, 30, 46]. Since Si_3N_4 has low Raman response [23], therefore, it is ignored during simulation by modifying the GNLSE equation as mentioned in [22]. The detailed simulation procedure, which is described in [21, 23], are followed. To avoid the spurious solution during simulation higher-order dispersion $\beta(w)$ up to 12th order are considered.

To test the phase stability of the simulated SC spectra, the modulus of complex degree of first-order coherency ($|g_{12}^{(1)}(\lambda)|$) is tested by considering quantum short noise one photon per bin by following the procedure described in [48, 49, 50, 51]:

$$|g_{12}^{(1)}(\lambda)| = \frac{\langle E_1^*(\lambda)E_2(\lambda)\rangle}{[\langle|E_1(\lambda)|^2\rangle \langle|E_2(\lambda)|^2\rangle]^{1/2}}. \quad (5)$$

where the angular brackets indicate an ensemble average of independently generated pairs $[E_1(\lambda), E_2(\lambda)]$ of SC spectra.

3

Table 2: **Fresnel reflection and mode profile mismatch losses calculated at the cascade point**

GVD Region	Cascade Structure	Fresnel Reflection Loss [dB]	Mode Field Mismatch Loss [dB]
All-anomalous	Air–SNW & ChG	0.1145	0.0431
All-anomalous	Silica–SNW & ChG	0.0958	0.1348
Normal to anomalous	Air–SNW & ChG	0.1579	0.5704
Normal to anomalous	Silica–SNW & ChG	0.1407	0.6737
All-normal	Air–SNW & ChG	0.1608	0.4835
All-normal	Silica–SNW & ChG	0.1434	0.6228

3. Results and Discussion

The proposed 8-mm-long cascade waveguide, whose initial segment is made of Si_3N_4 and the final segment is made of As_2Se_3 glass system, has been optimized for 2S-SC generation far into the MIR by considering commercially feasible pump source at the telecom wavelength of 1550 nm. The first waveguide segment is 6-mm-long and the final waveguide segment is 2-mm-long. Befo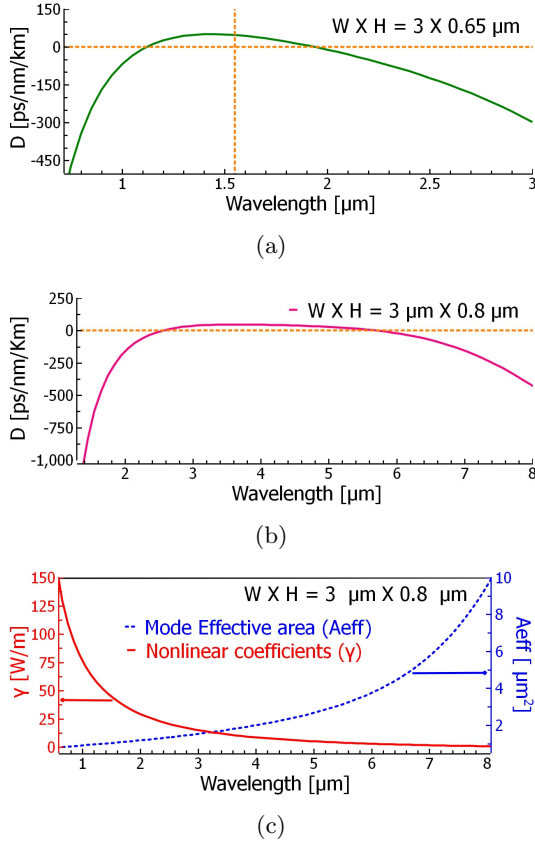re concatenating, both the structures are tailored and are made suitable for pulse propagation in either of anomalous or normal GVD region separately. Based on whether the pump is to employ in the anomalous or in the normal GVD regime, three different cascaded structures have been proposed and investigated for MIR SC generation by two-step pulse propagation process as follows: i) All-anomalous GVD regions 2S-SC generation; ii) Normal to anomalous GVD regions 2S-SC generation; and iii) All-normal GVD regions 2S-SC generation. In each case, cascade design between Air–SNW and ChGW is analyzed first and then investigation has been carried out for the cascade structure between Silica–SNW and ChGW segments.

3.1. All-anomalous GVD regions 2S-SC generation in cascade waveguide

To investigate spectral coverage far into the MIR, the initial SNW segment considering air as an upper cladding is optimized for pumping in the anomalous GVD region. To attain the zero-dispersion wavelength (λ_{ZDW}) vicinity to the wavelength selected for pumping the initial waveguide section at 1550 nm for 1st-step SC generation, the waveguide structure, $W = 3\ \mu m$ and $H = 0.65\ \mu m$ has been

(a)

(b)

(c)

Figure 2: Tailored GVD curves, wavelength dependent $A_{eff}(\omega)$ and its corresponding $\gamma(\omega)$ (final waveguide segment) for all-anomalous GVD regions 2S-SC generation in cascade waveguide: (a) GVD curve optimized for Air–SNW segment for pumping at 1550 nm wavelength; (b) GVD curve optimized for final segment, ChGW; and (c) $A_{eff}(\omega)$ and $\gamma(\omega)$ plots up to the desired wavelength for the final waveguide segment of the cascade waveguide.
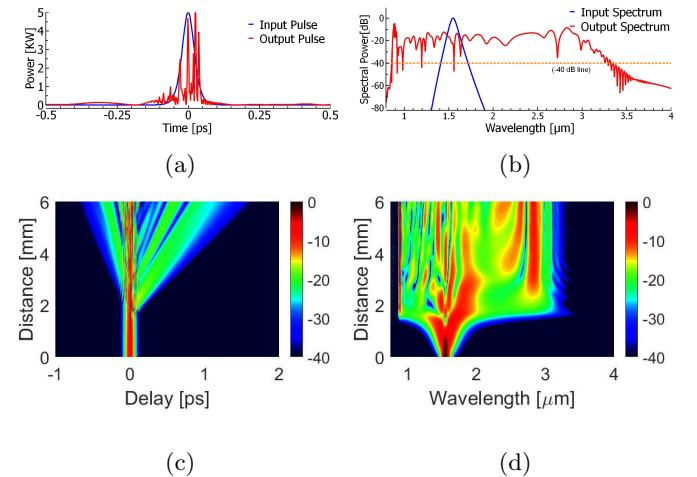

(a)   (b)

(c)   (d)

Figure 3: All-anomalous GVD region 1st-step SC generation by pumping the initial Air-SNW segment of cascade waveguide at 1550 nm wavelength: (a) Pulse intensity at the input and output end of the segment; (b) Spectrum at the input and output end of the segment; (c) Temporal profile along the 6-mm-long segment; and (d) Spectral density plot along the length of segment.
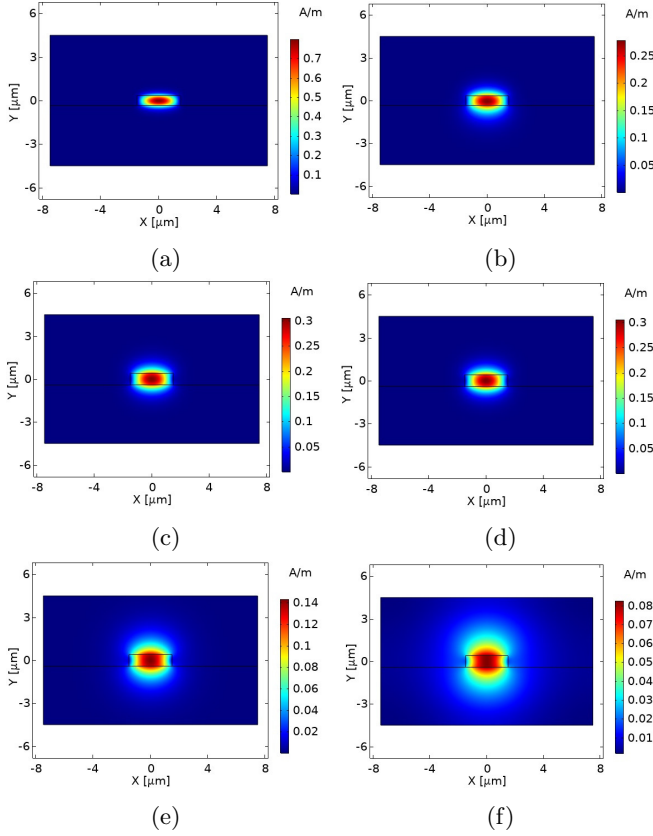
Figure 4: All-anomalous GVD region FQTE mode-field profiles (H_y^{11}) for Air–SNW & ChGW cascade waveguide plotted at: (a) 1.55 μm; (b) 3 μm; (c) 2.5 μm; (d) 5 μm; (e) 7.5 μm; and (f) 10 μm. Subplots (a)–(b) for initial waveguide segment and (c)–(d) for final segment of the cascade structure proposed.

optimized from several dimensional variations. The dispersion profile for the initial Air–SNW segment is illustrated in Fig. 2(a). From Fig. 2(a), the 1st λ_{ZDW} is obtained at 1.12 μm and the 2nd λ_{ZDW} is crossed from anomalous to normal GVD region at 1.94 μm. The GVD, D is calculated as 47.25 ps/nm/km at 1550 nm and at this wavelength the estimated values of A_{eff} and γ are recorded as 1.602 μm^2 and 0.633 W/m, respectively. The average propagation losses are taken as 2.5 dB/cm including material absorption loss, coupling and other reflection/refraction losses incurred at the cascade point during the simulations throughout. Detailed loss values calculated at the cascade point for the various optimized cascade designs considering different GVD regions are depicted in Table 2. Wavelength dependent nonlinear coefficients ($\gamma(\omega)$) are used throughout all the simulations carried out in this work. Now, a TE polarized (full-width half- maximum, T_{FWHM}= 50 fs, peak power, P_{p} = 5 kW) secant pulse at the chosen pump wavelength is launched into the Air–SNW section (initial segment) of the cascade waveguide. The pulse intensity at the input and output end of the 6-mm-long structure is illustrated in Fig. 3(a). The spectral coverage is shown in Fig. 3(b). The temporal and spectral profiles for this segment are depicted in Fig. 3(c) and Fig. 3(d), respec-
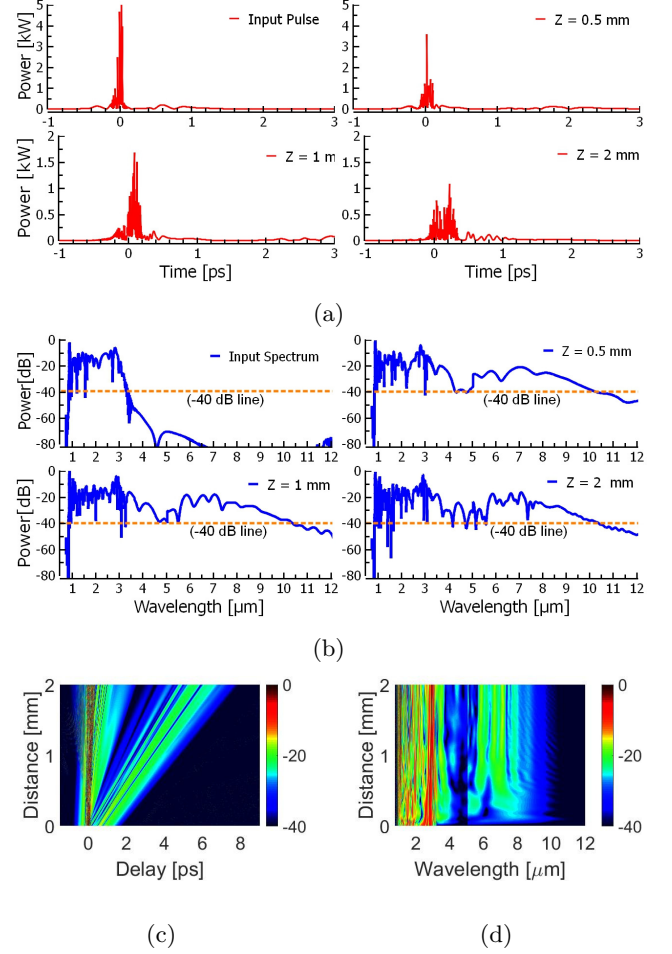

Figure 5: All-anomalous GVD region SC generation along the final waveguide segment: (a) Pulse intensities at the different length of ChGW; (b) Spectral coverage estimated at the different length of ChGW after an input given from initial Air-SNW segment; (c) Temporal evolution along the length of ChGW; and (d) Spectral density evolution along the length of ChGW.

tively. From spectral and temporal profiles, the soliton fission length, L_{fiss} can be estimated at 2.06 mm. From Figs. 3(b) and 3(d), it can be clearly seen that the 1st-step SC coverage can be predicted the range from 860 nm to 3257 nm [-40 dB equivalent].

The pulse obtained at the end of Air–SNW segment is needed to couple into the input of the 2nd segment of the cascade waveguide, ChGW. During coupling the amplifier stage is ignored. The 2nd step and final spectral coverage is completely relied on soliton self-frequency shift (SSFS) inside the 2nd segment of the cascade design. To see the further spectral extension keeping SSFS continuing in the second waveguide section, the final ChGW segment is tailored by the concepts discussed in [26, 31, 36]. Since the long wavelength SC spanning end of the Air–SNW is 3.257 μm, the 2nd and final waveguide segment, ChGW has been optimized to obtain a suitable anomalous GVD region by varying its H and W in such a way that the 1st λ_{ZDW} of this segment can be obtained below 3.257 μm so that
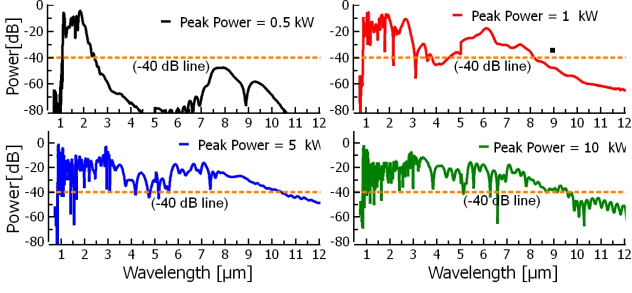
Figure 6: All-anomalous GVD regions spectral coverages with different peak power variations at the output of 8-mm-long Air–SNW and ChGW cascade waveguide.

it could be closer to the 2nd λ_{ZDW} of Air–SNW. By following these criteria, the 2nd waveguide segment, ChGW has been optimized with structural dimension, $W = 3$ μm and $H = 0.8$ μm. The tailored anomalous GVD profile for this waveguide segment and its corresponding wavelength dependent mode effective areas $(A_{eff}(\omega))$ and nonlinear coefficients $(\gamma(\omega))$ up to the suitable wavelength region are illustrated in Figs. 2(b) and 2(c), respectively. The FQTE mode profiles including two from initial waveguide segment at 1.55 μm and 3 μm, four from final segment at 2.5 μm, 5 μm, 7.5 μm and 10 μm are also depicted in Fig. 4. The obtained field profiles with different wavelength show excellent mode confinements for the cascade design. The values of A_{eff} and γ at the pump wavelength are calculated as 1.39 μm^2 and 18.71 W/m, respectively. From the anomalous GVD curve illustrated in Fig. 2(b), the 1st λ_{ZDW} is achieved at 2.56 μm and the 2nd λ_{ZDW} is crossed at 5.7 μm. The pulse intensities and the spectral coverages at the four different length of the 2-mm-long ChGW are illustrated in Figs. 5(a) and 5(b), respectively. The temporal and spectral density profiles along the 2-mm length of the final waveguide section are also illustrated in Figs. 5(c) and 5(d), respectively. Finally, it can be observed that owing to enhanced SSFS inside the final segment of the cascade structure, the SC coverage can be predicted up to 10 μm with a bandwidth in the range 0.86–10 μm at the output of cascade design between Air–SNW and ChGW.

An interesting phenomenon is observed during initial Air–SNW segment optimization for all-anomalous region 2S-SC generation. To obtain sufficient MIR SC extension
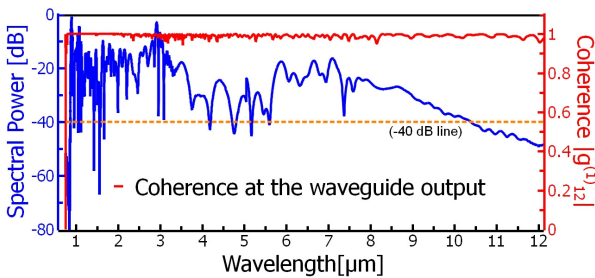
at the cascade structure output, initial segment must be tailored in such a way that its anomalous GVD region between 1st λ_{ZDW} and 2nd λ_{ZDW} should not be so large or so small in the wavelength range. To observe the situation described as well as to obtain minimum coupling loss at the cascade point, we have tested and optimized a few more Air–SNW structures raising H near to the H of 2nd waveguide segment which result in deterioration of SC expansion not only at the Air–SNW output but also at the cascade structure output as well. Larger H increases the range of anomalous GVD region resulting in reduction of solitons energy due to longer wavelength region propagation. On the other hand, decreasing H and W reduce the anomalous GVD region so small that the expansion at the Air–SNW output falls substantially. Thus, 1st waveguide segment should be optimized in a manner that higher-order solitons are able to propagate inside of it with enough energy up to the cascade point and then enter into the 2nd waveguide segment via coupling. As a consequence, the higher-order solitons with sufficient energy, during propagation inside the 2nd waveguide segment, can interact with larger γ which enhance the SSFS that eventually yields the sufficient MIR extension at the cascade structure output.

The effect of P_p variations on the SC coverage at the output of Air–SNW and ChGW is demonstrated in Fig. 6. Increasing P_p from 0.5 kW to 10 kW enhances the flatness of the evolved SC coverage rather than further extension.
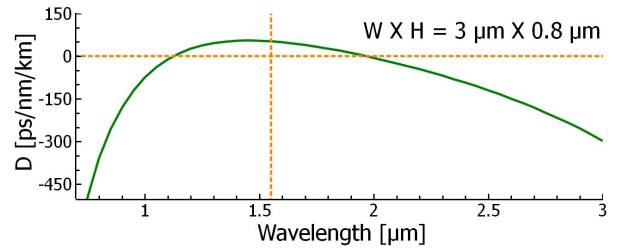
(a)
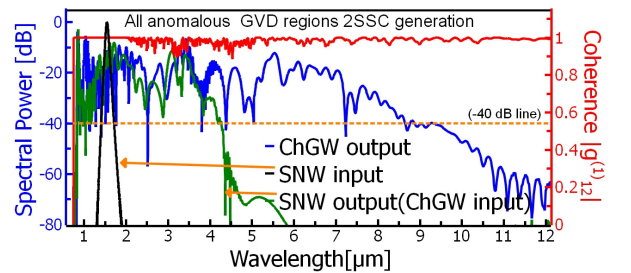
(b)

Figure 8: All-anomalous GVD regions 2S-SC generation for Silica–SNW and ChGW cascade structure: (a) GVD curve is optimized for Silica–SNW segment considering pump at 1550 nm wavelength in the anomalous GVD regime; and (b) Spectral coverages are estimated at the input (solid-black curve), at the cascade point (solid-green curve), and at the output (solid-blue line) of cascade waveguide. Also first degree of coherence ($|g_{12}|$) is shown by solid-red line at the cascade waveguide output.

Figure 7: Coherence at the output of Air–SNW and ChGW cascade waveguide for all-anomalous GVD regions 2S-SC generation.

The coherence of the spectrum obtained using 5 kW peak power is analyzed and is illustrated in Fig. 7. The estimated values of degree of coherence, $|g_{12}|$ up to the entire SC coverage region, as it maintains near unity up to SC bandwidth predicted, suggested that the obtained SC is highly coherent.

The MIR spectral coverage is next investigated of the cascade waveguide replacing top air cladding of initial SNW segment by SiO_2 keeping the final ChGW structure ($W \times H$ = 3 μm $\times$ 0.8 μm) same as before. According to the approach followed earlier, the Silica–SNW segment is tailored with a structure of $W \times H$ = 3 μm $\times$ 0.8 μm for anomalous GVD region pumping considering pump operating at 1550 nm wavelength. The optimized GVD curve for this waveguide segment is illustrated in Fig. 8(a). It is apparent from Fig. 8(a) that the 1st λ_{ZDW} is obtained at 1.18 μm and the 2nd λ_{ZDW} which again goes back to the normal GVD region at 2.23 μm. The obtained D, A_{eff}, and γ for this segment at 1550 nm are 54.71 ps/nm/km, 1.91 μm^2, and 0.5295 W/m, respectively. For ChGW segment, the GVD curve tailored in Fig. 2(b) is kept same with all simulation parameters obtained and considered during cascading with Air-SNW segment. After concatenating between Silica–SNW and ChGW, a TE polarized sech pulse with the same pulse parameters is applied into the input of cascade design. The output spectrum obtained at the end of Silica–SNW is illustrated as solid-green-line curve in Fig. 8(b) with a long wavelength extension up to 4200 nm. The output pulse is then coupled as an input of ChGW segment. The pulse is propagated in the 2nd waveguide section with SSFS, which eventually enhance the pulse spectrum further into the MIR. As solid-blue line curve shown in Fig. 8(b), the SC spectrum expands up to 8650 nm with a bandwidth in the range 830–8650 nm. In this case, more flat coverage up to 7200 nm can be observed compared to the spectral coverage predicted by the cascade design made of Air–SNW and ChGW segments. The $|g_{12}|$ calculated, as shown in Fig. 8(b) with solid-red-line, with unity over the entire spectral outcome proves that the output spectrum obtained using all-anomalous GVD regions cascade design between Silica–SNW and ChGW is highly coherent. The main advantage of cascade design between Silica–SNW and ChGW over Air–SNW and ChGW is that both the segments of Silica–SNW and ChGW have been optimized with same structural thickness H, which is very crucial for reducing the coupling loss at the cascade point significantly. Especially, obtaining equal H, as it provides the significant reduction of coupling losses, should be the prime target during cascade waveguide design.

3.2. Normal to anomalous GVD regions 2S-SC generation in cascade waveguide

To observe normal to anomalous GVD region SC generation at the output of a cascade design, initial waveguide section, Air–SNW is tailored and made suitable for all normal dispersion pumping at the chosen wavelength in such as way that the minimum GVD point of all-normal
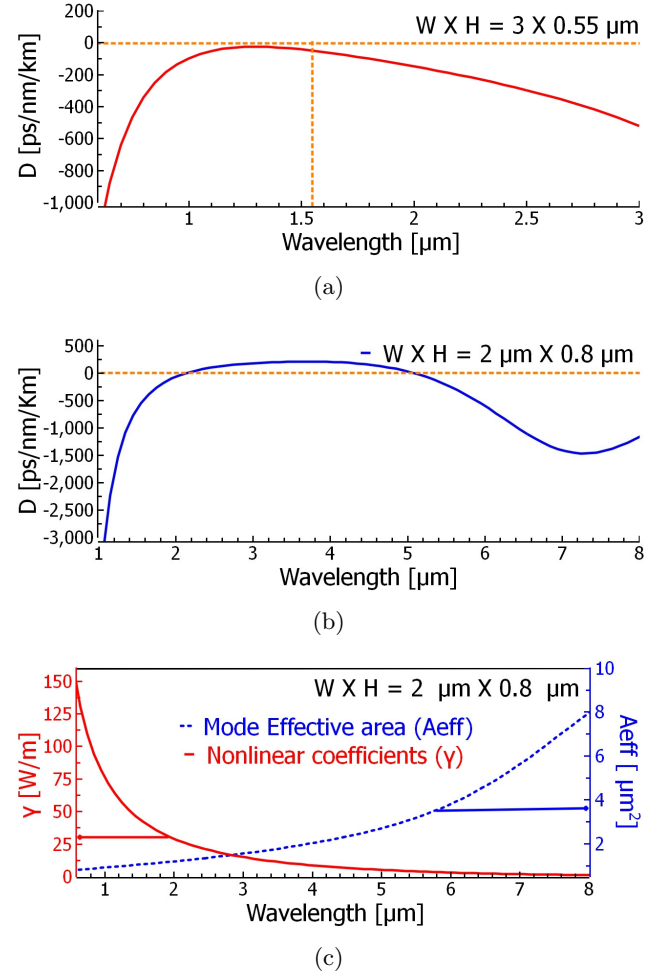

Figure 9: Tailored GVD curves, wavelength dependent $A_{eff}(\omega)$ and its corresponding $\gamma(\omega)$ (final waveguide segment) for normal to anomalous GVD regions 2S-SC generation in cascade waveguide: (a) GVD curve optimized for Air–SNW segment for pumping at 1550 nm wavelength; (b) GVD curve optimized for final segment, ChGW; and (c) $A_{eff}(\omega)$ and $\gamma(\omega)$ plots up to the desired wavelength for the final waveguide segment of the cascade waveguide.

dispersion GVD curve should be located around 1550 nm wavelength. After a number of Air–SNWs analyzed, the optimized structure, W = 3 μm and H = 0.55 μm has been selected for 1st-step SC generation and the tailored all-normal dispersion GVD curve for this waveguide section is illustrated in Fig. 9(a). It is apparent from all-normal dispersion GVD curve depicted in Fig. 9(a) that the minimum GVD point is obtained near to the chosen pump wavelength which is expected for 1st-step SC coverage by Air–SNW in normal to anomalous dispersion region 2S-SC generation. The calculated values of A_{eff}, γ, and D at 1550 nm wavelength for the initial waveguide segment are 1.48 μm^2, 0.6833 W/m, -50.68 ps/nm/km respectively. Now, a TE polarized secant pulse with a pulse peak power of 5 kW is launched into this waveguide segment and the spectral coverage for all-normal dispersion output is illustrated in Fig. 10. The estimated spectrum
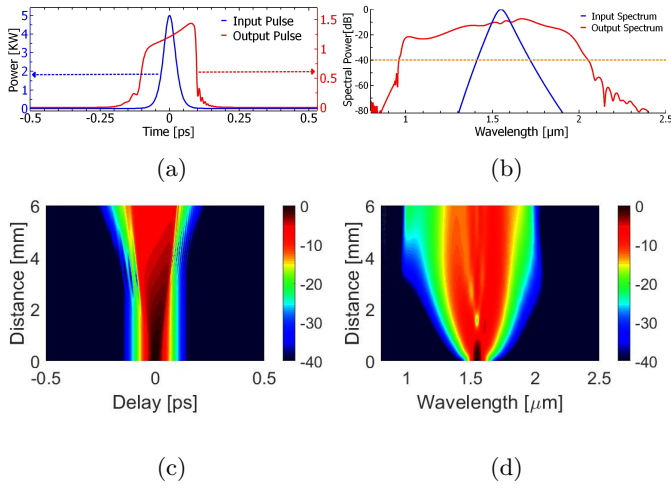
Figure 10: Normal GVD region 1st-step SC generation by pumping the initial Air-SNW section of cascade waveguide at 1550 nm wavelength: (a) Pulse intensity at the input and output end of the segment; (b) Spectrum at the input and output end of the segment; (c) Temporal profile along the 6-mm-long segment; and (d) Spectral density plot along the whole length of the segment.
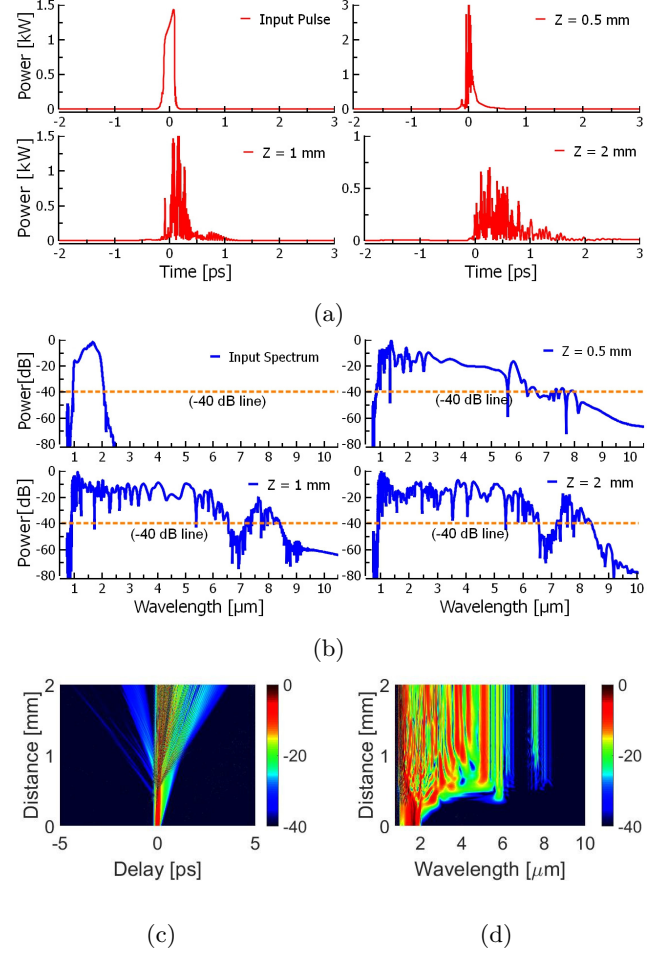

Figure 11: Anomalous GVD region SC generation along the length of final waveguide segment: (a) Pulse intensities at the different length of ChGW; (b) Anomalous dispersion spectral coverage estimated at the different length of ChGW after an input is given from an initial segment; (c) Temporal evolution along the length of ChGW; and (d) Spectral density evolution along the length of ChGW.

covers the wavelength region 962–2050 nm [-40 dB equivalent]. Figure 10(a) shows the initial and final pulse intensities at the input and output end of 6-mm-long Air–SNW waveguide. Owing to all-normal dispersion pulse propagation, the pulse has been broadened at the output end of this waveguide segment. The input and the output pulse spectrum are shown in Fig. 10(b). As expected, output spectrum does not broaden enough due to pumping this segment in the all-normal dispersion regime. Figures 10(c) and 10(d) show the corresponding temporal and spectral density plots of spectrum predicted in Fig. 10(b).

Next, cascading between Air–SNW and ChGW is carried out using a similar approach followed in the earlier section. Before concatenating, based on the long wavelength SC coverage end predicted by the initial waveguide segment, the ChGW is needed to be optimized in such a manner that the output pulse from the initial segment must be received by the ChGW in the anomalous dispersion regime. Based on this fact, the ChGW has been tailored with a structure, W= 2 μm and H = 0.8 μm in such that the 1st λ_{ZDW} is at obtain at 2.13 μm and 2nd λ_{ZDW} is at 5.08 μm. The GVD curve and and its corresponding wavelength dependent A_{eff} and γ are illustrated in Figs. 9(b) and 9(c), respectively. It is apparent from Fig. 9(b) that nearly flat anomalous dispersion region GVD curve is achieved as expected. The output normal dispersion broadened pulse from Air–SNW can now be coupled with the optimized ChGW where the incoming pulse from 1st-waveguide segment starts to propagate inside the 2-mm-long 2nd-waveguide segment in the anomalous GVD regime. As expected, soliton fission starts around 0.2 mm along the length of ChGW due to pulse propagating in the anomalous dispersion regime. A number of fundamental solitons are induced by breaking the

pulse after 0.2 mm which are then red-shifted owing to SSFS and their evolutions can be clearly observed at various locations illustrated along the 2-mm waveguide length in Fig. 11(a). The spectral evolutions at the output of ChGW corresponding to these pulse propagations are depicted in Fig 11(b) and the spectral coverage, in this case, is predicted in the range 908–6500 nm [-40 dB equivalent]. In this case, it can be observed spectral coverage expanded up to 8400 nm, however, a dip between 6500 nm and 7500 nm is induced, whose spectral power falls down below -40 dB. The temporal and spectral density plots along the 2-mm length of the final segment of the waveguide are shown in Figs. 10(c) and 10(d), respectively.

The effect of P_p variations on the spectral coverage at the output of Air–SNW and ChGW, in the case of normal to anomalous dispersion region 2S-SC generation, is illustrated in Fig. 12. It can be observed P_p variations from 0.5 kW to 10 kW that increasing power enhances the flatness of the spectral coverage rather than further spec-
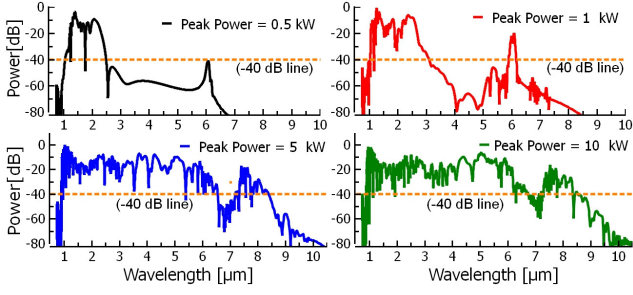
Figure 12: Normal to anomalous GVD regions spectral coverages with different peak power variations at the output of 8-mm-long Air–SNW and ChGW cascade waveguide.

tral extension. The degree of coherence of the spectrum obtained using 5 kW peak power is analyzed and is illustrated in Fig. 13. Slightly deteriorated coherency can be observed around 1.5 μm, other than, the estimated values of $|g_{12}|$ up to the remaining SC coverage implies highly coherent.

To observe MIR coverage at the cascade waveguide output by replacing air with SiO_2 of the initial waveguide segment in the cascade structure proposed in this section earlier, initial segment is optimized with a structure $W \times H = 2~\mu m \times 0.6~\mu m$ by varying its transverse dimensions. The tailored GVD curve for this structure is depicted in Fig. 14(a) and the GVD value obtained at the pump wavelength is close to the minimum GVD value of this design. The parameters D, A_{eff}, and γ for this segment at 1550 nm are calculated -73.3 ps/nm/km, 1.666 μm^2, and 0.6083 W/m, respectively. For convenience, as we have optimized Silica–SNW segment based on ChGW segment optimized for cascade design between Air–SNW and ChGW earlier, we keep the structural dimensions of the 2nd cascade segment made of ChGW same, which was $W \times H = 2~\mu m \times 0.8~\mu m$ and whose GVD curve was illustrated in Fig. 9(b). Required various simulation parameters relevant to this segment are taken from the ChGW segment optimized earlier for Air–SNW and ChGW cascade structure. Applying previous approach with various parameters set for SC simulations, a TE polarized sech pulse is launched into the input of this structure and pulse spectrum at the various points of the cascade waveguide is shown in Fig. 14(b). Pulse spectrum at the input, at the
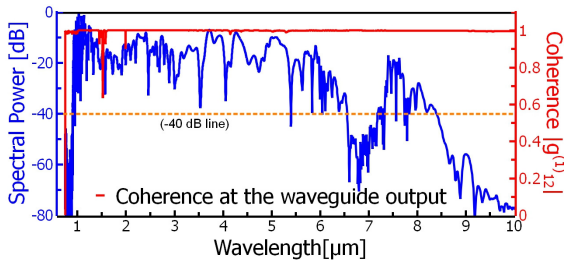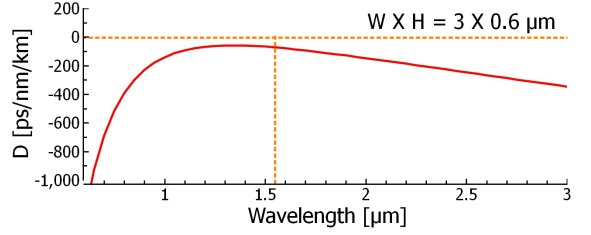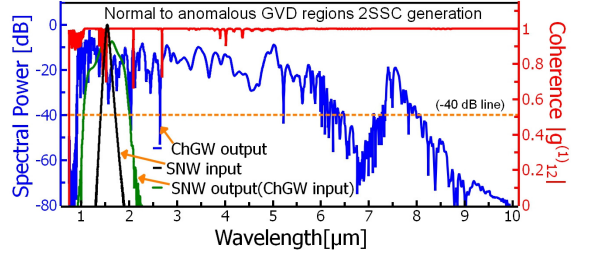

Figure 13: Coherence at the output of Air–SNW and ChGW cascade waveguide for normal to anomalous GVD regions 2S-SC generation.


(a)

(b)

Figure 14: Normal to anomalous GVD regions 2S-SC generation for Silica–SNW and ChGW cascade structure: (a) GVD curve is optimized for Silica–SNW segment considering pump at 1550 nm wavelength in the normal GVD regime; and (b) Spectral coverages are estimated at the input (solid-black curve), at the cascade point (solid-green curve), and at the output (solid-blue line) of cascade waveguide. Also degree of coherence ($|g_{12}|$) is shown by solid-red line at the cascade waveguide output.

cascade point, and at the output of the cascade waveguide shown in Fig. 14(b) are indicated by solid-black, solid-green, and solid-blue curves, respectively. Spectral coverage up to 6400 nm can be predicted by the Silica–SNW and ChGW cascade structure optimized for pulse propa-
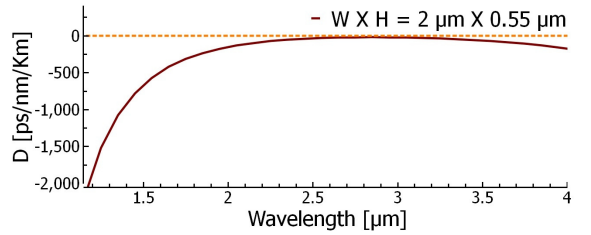
(a)
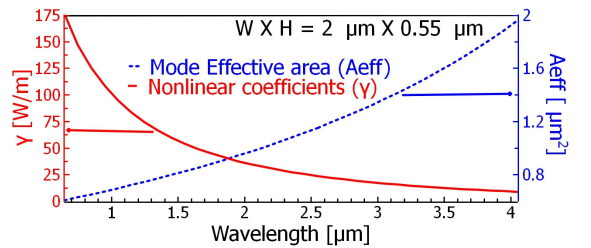
(b)

Figure 15: All-normal dispersion (a) GVD curve optimized for the final segment, ChGW; and (b) $A_{eff}(\omega)$ and $\gamma(\omega)$ plots up to the desired wavelength for the final segment of the cascade waveguide.

gating in the normal to anomalous GVD regimes. In addition to this, a dip is appeared between 6500–7500 nm and again rises the spectral power above -40 dB line until 8000 nm. The spectral coherence, which is presented using solid-red line in Fig. 14(a), $|g_{12}|$ can be obtained unity over the entire spectral coverage except somewhat deterioration around 1500 nm wavelength.

3.3. All-normal GVD regions 2S-SC generation in cascade waveguide

The 2S-SC generation for all-normal dispersion optimized cascade design is investigated here. All-normal dispersion GVD curve for the initial segment Air–SNW, which was illustrated in Fig. 9(a), is kept same and the structure optimized for this purpose was $W = 2~\mu m$ and $H = 0.55~\mu m$. The 2nd waveguide segment, ChGW with transverse dimension, $W = 2~\mu m$ and $H = 0.55~\mu m$ is also tailored for all-normal dispersion MIR SC coverage. The

Figure 17: All-normal GVD regions spectral coverages with different peak power variations at the output of 8-mm-long Air–SNW and ChGW cascade waveguide.

all-normal dispersion GVD curve for this structure is illustrated in Fig. 15(a) and Fig. 15(b) shows its corresponding wavelength dependent A_{eff} and γ plot. After cascading, a TE-polarized sech pulse with the same pulse width and peak power is applied into the input of the 6-mm-long Air–SNW segment at the chosen pump wavelength of 1550 nm. The detailed outcome for this waveguide segment was illustrated in Fig. 10. The output of this segment is now coupled with ChGW, which is optimized for all-normal dispersion pulse propagation too. The time domain pulse propagation at the various length of 2-mm-long ChGW is illustrated in Fig 16(a). As expected, the pulse broadened more and more with propagation along the length of the waveguide structure, which can clearly be observed from the various subplots shown in Fig. 16(a). Figure 16(b) shows the spectra at the different waveguide length corresponding to the pulse propagation depicted in Fig. 16(a). From this figure, it can be estimated all-normal dispersion flat SC spanning up to 3055 nm [-40 dB equivalent] by the cascade waveguide proposed. All-normal GVD temporal and spectral density profiles corresponding to the spectrum predicted at the cascade waveguide output are shown in Figs. 16(c) and 16(d), respectively. Flat spectral coverage may be obtained in case of all-normal dispersion pulse propagation along the 8-mm-long design between Air–SNW and ChGW. However, the MIR spectral expansion at the waveguide output has been reduced substantially compared to the cascade designs described earlier owing to the all-normal dispersion pumping and pulse propagation throughout the length of cascade waveguide
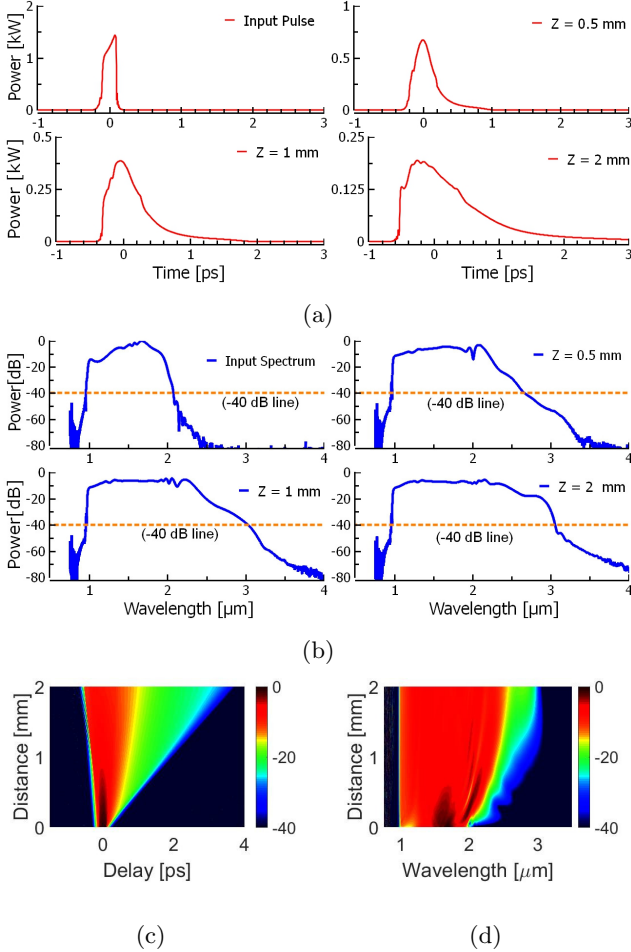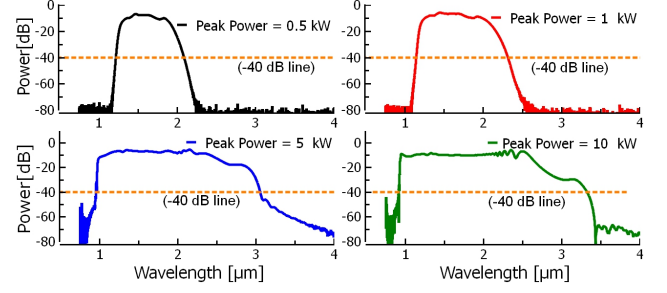

Figure 16: Normal GVD region SC generation along the length of final waveguide segment: (a) Pulse intensities at the four different positions along 2-mm length of ChGW; (b) Normal dispersion spectral coverages estimated at the four different length of ChGW waveguide after an input given from Air–SNW; (c) Temporal evolution along the length of ChGW; and (d) Spectral density evolution along the length of ChGW.
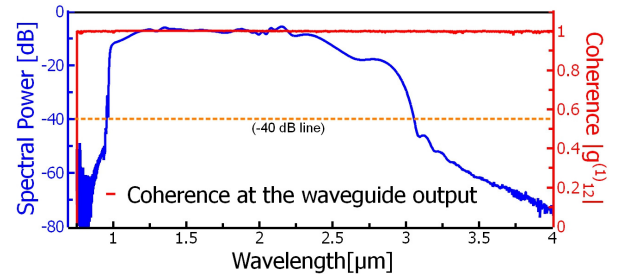

Figure 18: Coherence at the output of cascade waveguide for all-normal dispersion regions 2S-SC generation.

Table 3: **Comparison among SC coverages in different cases of dispersion region considered**

GVD Region	Air–SNW & ChGW SC Coverage	Silica–SNW & ChGW SC Coverage
All-anomalous	860 – 10000 nm	830 – 8650 nm
Normal to anomalous	908 – 6500 nm	913 – 6400 nm
All-normal	956 – 3055 nm	1000 – 3000 nm

proposed.

The effect of P_p variations with the four different peak powers are illustrated in Fig. 17. It is apparent from this figure that increasing power enhances the spectra further in the MIR. Spectrum increases up to 3400 nm if we double the input peak power, as shown in Fig. 17(d). However, flatness of the output spectra does not change as the input power increases. The degree of coherence for the dispersion-engineered all-normal dispersion cascade system is demonstrated in Fig. 18. It can be clearly observed from this figure that the estimated degree of coherence, $|g_{12}|$ has been maintained unity up to the entire spectral coverage obtained which implies the cascade waveguide we have proposed here for all-normal dispersion 2S-SC generation is highly coherent.

For all-normal GVD regions 2S-SC generation using design between Silica–SNW and ChGW, we utilize optimized silica–SNW structure $W \times H = 3$ μm $\times$ 0.6 μm from earlier section whose GVD curve was illustrated in Fig. 14(a). The optimized ChGW segment with structure $W \times H = 2$ μm $\times$ 0.55 μm, which was used for the cascading between Air–SNW and ChGW proposed earlier in this section, is used for a final segment, whose GVD curve was depicted in Fig. 15(a). Following the earlier approach, simulations are carried out using a TE polarized pulse with all required parameters as the input of a cascade structure optimized for the all-normal SC generation at the output. Figure 19 shows the all-normal GVD regions SC generation predicted at the various points of cascaded between Silica–SNW and ChGW structure proposed. Input pulse spectrum, spectrum at the cascade point, and the final spectral coverage from 1000 to 3000 nm at the waveguide output, as shown in Fig. 19, are indicated by black, green, and blue curves,
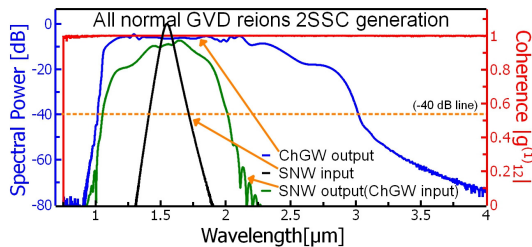
respectively. The estimation of $|g_{12}|$ over the entire final spectral coverage, which is indicated by solid-red line illustrated in this figure shows that the obtained SC is highly coherent.

3.4. Comparative analysis

Finally, a comparison among three different dispersion regions 2S-SC generation have been made in Fig. 20 and a comparison table, Table 3 have also been prepared with the numerical results predicted and obtained under three different GVD regions considered for the cascade waveguide proposed. Comparison among spectral coverages for the cascade structure between Air–SNW and ChGW as shown in Fig. 20(a) and the cascade structure between Silica–SNW and ChGW as shown in Fig. 20(b) are mentioned inside the table separately. We can state, among the three spectra illustrated either in Fig. 20(a) or in Fig. 20(b), that the highest SC coverage up to 10000 nm can be predicted by the Air–SNW and ChGW cascade design. However, comparatively more flat MIR coverage up to 8650 nm can be obtained by the other design made of Silica–SNW and ChGW cascade design. These wide spectral coverages up to the MIR have become possible through the all-anomalous GVD regions 2S-SC generation using a 1550
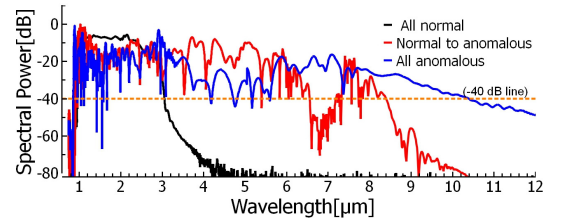
(a)
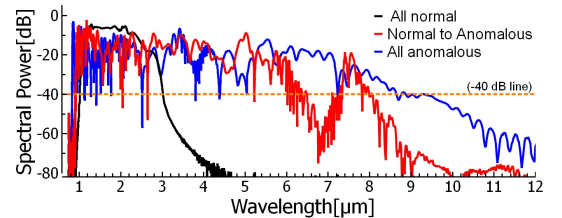
(b)

Figure 20: Comparison among SC spectra predicted and obtained using three different GVD regions considered: (a) at the output of Air–SNW and ChGW cascade structure; and (b) at the output of Silica–SNW and ChGW cascade structure.

Figure 19: All-normal GVD regions 2S-SC generation for Silica–SNW and ChGW cascade structure. Spectral coverages are estimated at the input (solid-black curve), at the cascade point (solid-green curve), and at the output (solid-blue line) of cascade waveguide. Also degree of coherence ($|g_{12}|$) is shown by solid-red line at the cascade waveguide output.

11

nm telecom wavelength commercially available femtosecond pump source with a moderate peak power of 5 kW.

4. Concluding remarks

In this work, we numerically demonstrate the MIR SC generation from 0.86 to 10 μm using a 8-mm-long cascade waveguide optimized for pumping in commercially available telecom wavelength pump source operating at a wavelength of 1550 nm with a moderate peak power of 5 kW. Cascade waveguide proposed here consists of two waveguide segments that are made either of Air–Si$_3$N$_4$ (Air–SNW) or SiO$_2$–Si$_3$N$_4$ (Silica–SNW) and As$_2$Se$_3$ (ChGW) glass systems. The waveguide structure is tailored for three different GVD regions 2S-SC generation. Initial waveguide segment, SNW is simulated considering the pulse emitting from the chosen telecom wavelength pump source. The output pulse from SNW structure is then coupled into the 2nd waveguide, ChGW. Based on the long wavelength spectral expansion end of initial waveguide segment, the dispersion region of the 2nd waveguide segment has been tailored. Pulse propagation dynamics inside the 2nd waveguide structure depend on whether the anomalous or normal GVD region achieved. In this way, using two-step SC generation, the MIR spectral coverage can be predicted by choosing the telecom wavelength pump source at 1550 nm. The MIR spectral coverage obtained by the two-step process (2S-SC) may not be possible by a single-step conventional SC generation using the commercially available telecommunication wavelength pump source proposed. However, coupling, mode-area mismatch, Fresnel and other reflection/refraction losses at the coupling point will incur higher than the losses considered here, which may be minimized by using a amplifier stage between the cascade point. Finally spectral coherence of the proposed waveguide has been tested and found to be highly coherent SC coverage for the entire wavelength region achieved. Such a highly coherent broad SC spectrum can be suitable for many applications in the fields of sensing and biological imaging and to be particular in ultrafast absorption spectroscopy, optical coherent tomography, etc.

References

[1] C. R. Petersen, M. B. Lotz, G. Woyessa, A. N. Ghosh, T. Sylvestre, L. Brilland, J. Troles, M. H. Jakobsen, R. Taboryski, O. Bang, Nanoimprinting and tapering of chalcogenide photonic crystal fibers for cascaded supercontinuum generation, Optics Letters 44 (22) (2019) 5505–5508.

[2] S. Wartewig, R. H. H. Neubert, Pharmaceutical applications of mid-ir and raman spectroscopy, Advanced drug delivery reviews 57 (8) (2005) 1144–1170.

[3] A. B. Seddon, Mid-infrared (ir)–a hot topic: The potential for using mid-ir light for non-invasive early detection of skin cancer in vivo, Physica Status Solidi (b) 250 (5) (2013) 1020–1027.

[4] R. Haus, K. Schäfer, W. Bautzer, J. Heland, H. Mosebach, H. Bittner, T. Eisenmann, Mobile fourier-transform infrared spectroscopy monitoring of air pollution, Applied Optics 33 (24) (1994) 5682–5689.

[5] A. Mukherjee, S. Von der Porten, C. K. N. Patel, Standoff detection of explosive substances at distances of up to 150 m, Applied Optics 49 (11) (2010) 2072–2078.

[6] I. Zorin, R. Su, A. Prylepa, J. Kilgus, M. Brandstetter, B. Heise, Mid-infrared fourier-domain optical coherence tomography with a pyroelectric linear array, Optics Express 26 (25) (2018) 33428–33439.

[7] C. Amiot, A. Aalto, P. Ryczkowski, J. Toivonen, G. Genty, Cavity enhanced absorption spectroscopy in the mid-infrared using a supercontinuum source, Applied Physics Letters 111 (6) (2017) 061103.

[8] C. R. Petersen, N. Prtljaga, M. Farries, J. Ward, B. Napier, G. R. Lloyd, J. Nallala, N. Stone, O. Bang, Mid-infrared multi-spectral tissue imaging using a chalcogenide fiber supercontinuum source, Optics Letters 43 (5) (2018) 999–1002.

[9] J. Hult, R. S. Watt, C. F. Kaminski, High bandwidth absorption spectroscopy with a dispersed supercontinuum source, Optics Express 15 (18) (2007) 11385–11395.

[10] C. R. Petersen, U. Møller, I. Kubat, B. Zhou, S. Dupont, J. Ramsay, T. Benson, S. Sujecki, N. Abdel-Moneim, Z. Tang, et al., Mid-infrared supercontinuum covering the 1.4–13.3 μm molecular fingerprint region using ultra-high na chalcogenide step-index fibre, Nature Photonics 8 (11) (2014) 830–834.

[11] Y. Wu, M. Meneghetti, J. Troles, J.-L. Adam, Chalcogenide microstructured optical fibers for mid-infrared supercontinuum generation: interest, fabrication, and applications, Applied Sciences 8 (9) (2018) 1637.

[12] A. B. Seddon, Biomedical applications in probing deep tissue using mid-infrared supercontinuum optical biopsy, Deep Imaging in Tissue and Biomedical Materials: Using Linear and Nonlinear Optical Methods (2017) 231.

[13] A. N. Ghosh, M. Klimczak, R. Buczynski, J. M. Dudley, T. Sylvestre, Supercontinuum generation in heavy-metal oxide glass based suspended-core photonic crystal fibers, JOSA B 35 (9) (2018) 2311–2316.

[14] F. Belli, A. Abdolvand, W. Chang, J. C. Travers, P. S. J. Russell, Vacuum-ultraviolet to infrared supercontinuum in hydrogen-filled photonic crystal fiber, Optica 2 (4) (2015) 292–300.

[15] T. Cheng, K. Nagasaka, T. H. Tuan, X. Xue, M. Matsumoto, H. Tezuka, T. Suzuki, Y. Ohishi, Mid-infrared supercontinuum generation spanning 2.0 to 15.1 μm in a chalcogenide step-index fiber, Optics Letters 41 (9) (2016) 2117–2120.

[16] A. Lemiere, F. Désévédavy, P. Mathey, P. Froidevaux, G. Gadret, J.-C. Jules, C. Aquilina, B. Kibler, P. Béjot, F. Billard, et al., Mid-infrared supercontinuum generation from 2 to 14 μm in arsenic-and antimony-free chalcogenide glass fibers, JOSA B 36 (2) (2019) A183–A192.

[17] P. Lucas, Z. Yang, M. K. Fah, T. Luo, S. Jiang, C. Boussard-Pledel, M.-L. Anne, B. Bureau, Telluride glasses for far infrared photonic applications, Optical Materials Express 3 (8) (2013) 1049–1058.

[18] Z. Zhao, B. Wu, X. Wang, Z. Pan, Z. Liu, P. Zhang, X. Shen, Q. Nie, S. Dai, R. Wang, Mid-infrared supercontinuum covering 2.0–16 μm in a low-loss telluride single-mode fiber, Laser & Photonics Reviews 11 (2) (2017) 1700005.

[19] H. Hu, X. Zhang, W. Li, N. K. Dutta, Simulation of octave spanning mid-infrared supercontinuum generation in dispersion-varying planar waveguides, Applied Optics 54 (11) (2015) 3448–3454.

[20] X. Zhang, H. Hu, W. Li, N. K. Dutta, Mid-infrared supercontinuum generation in tapered As$_2$S$_3$ chalcogenide planar waveguide, Journal of Modern Optics 63 (19) (2016) 1965–1971.

[21] M. R. Karim, B. M. A. Rahman, G. P. Agrawal, Mid-infrared supercontinuum generation using dispersion-engineered Ge$_{11.5}$As$_{24}$Se$_{64.5}$ chalcogenide channel waveguide, Optics Express 23 (5) (2015) 6903–6914.

[22] M. R. Karim, N. Al Kayed, M. R. Hossain, B. M. A. Rahman, Study of low-peak-power highly coherent broadband supercontinuum generation through a dispersion-engineered si-rich silicon nitride waveguide, Applied Optics 59 (20) (2020) 5948–5956.

[23] H. Ahmad, M. R. Karim, B. M. A. Rahman, Dispersion-engineered silicon nitride waveguides for mid-infrared supercontinuum generation covering the wavelength range 0.8–6.5 μm, Laser Physics 29 (2) (2019) 025301.

[24] Y. Yu, X. Gai, T. Wang, P. Ma, R. Wang, Z. Yang, D.-Y. Choi, S. Madden, B. Luther-Davies, Mid-infrared supercontinuum generation in chalcogenides, Optical Materials Express 3 (8) (2013) 1075–1086.

[25] M. Bache, H. Guo, B. Zhou, Generating mid-IR octave-spanning supercontinua and few-cycle pulses with solitons in phase-mismatched quadratic nonlinear crystals, Optical Materials Express 3 (10) (2013) 1647–1657.

[26] I. Kubat, C. R. Petersen, U. V. Møller, A. Seddon, T. Benson, L. Brilland, D. Méchin, P. M. Moselund, O. Bang, Thulium pumped mid-infrared 0.9–9μm supercontinuum generation in concatenated fluoride and chalcogenide glass fibers, Optics Express 22 (4) (2014) 3959–3967.

[27] J. Hu, C. R. Menyuk, L. B. Shaw, J. S. Sanghera, I. D. Aggarwal, Maximizing the bandwidth of supercontinuum generation in As_2Se_3 chalcogenide fibers, Optics Express 18 (7) (2010) 6722–6739.

[28] W. Yuan, 2–10 μm mid-infrared supercontinuum generation in As_2Se_3 photonic crystal fiber, Laser Physics Letters 10 (9) (2013) 095107.

[29] C. Wei, X. Zhu, R. A. Norwood, F. Song, N. Peyghambarian, Numerical investigation on high power mid-infrared supercontinuum fiber lasers pumped at 3 μm, Optics Express 21 (24) (2013) 29488–29504.

[30] J. M. Dudley, G. Genty, S. Coen, Supercontinuum generation in photonic crystal fiber, Reviews of Modern Physics 78 (4) (2006) 1135.

[31] S. Venck, F. St-Hilaire, L. Brilland, A. N. Ghosh, R. Chahal, C. Caillaud, M. Meneghetti, J. Troles, F. Joulain, S. Cozic, et al., 2–10 μm mid-infrared fiber-based supercontinuum laser source: Experiment and simulation, Laser & Photonics Reviews (2020) 2000011.

[32] Y. Tang, L. G. Wright, K. Charan, T. Wang, C. Xu, F. W. Wise, Generation of intense 100 fs solitons tunable from 2 to 4.3 μm in fluoride fiber, Optica 3 (9) (2016) 948–951.

[33] L.-R. Robichaud, V. Fortin, J.-C. Gauthier, S. Châtigny, J.-F. Couillard, J.-L. Delarosbil, R. Vallée, M. Bernier, Compact 3–8 μm supercontinuum generation in a low-loss As_2Se_3 step-index fiber, Optics Letters 41 (20) (2016) 4605–4608.

[34] H. P. T. Nguyen, K. Nagasaka, T. H. Tuan, T. S. Saini, X. Luo, T. Suzuki, Y. Ohishi, Highly coherent supercontinuum in the mid-infrared region with cascaded tellurite and chalcogenide fibers, Applied Optics 57 (21) (2018) 6153–6163.

[35] F. Théberge, N. Bérubé, S. Poulain, S. Cozic, S. Châtigny, L.-R. Robichaud, L.-P. Pleau, M. Bernier, R. Vallée, Infrared supercontinuum generated in concatenated InF_3 and As_2Se_3 fibers, Optics Express 26 (11) (2018) 13952–13960.

[36] C. R. Petersen, P. M. Moselund, C. Petersen, U. Møller, O. Bang, Mid-ir supercontinuum generation beyond 7 μm using a silica-fluoride-chalcogenide fiber cascade, in: Optical Biopsy XIV: Toward Real-Time Spectroscopic Imaging and Diagnosis, Vol. 9703, International Society for Optics and Photonics, 2016, p. 97030A.

[37] V. Shiryaev, M. Churbanov, Trends and prospects for development of chalcogenide fibers for mid-infrared transmission, Journal of Non-Crystalline Solids 377 (2013) 225–230.

[38] M. R. Karim, H. Ahmad, S. Ghosh, B. M. A. Rahman, Mid-infrared supercontinuum generation using As_2Se_3 photonic crystal fiber and the impact of higher-order dispersion parameters on its supercontinuum bandwidth, Optical Fiber Technology 45 (2018) 255–266.

[39] A. L. Gaeta, M. Lipson, T. J. Kippenberg, Photonic-chip-based frequency combs, Nature Photonics 13 (3) (2019) 158–169.

[40] K. Luke, Y. Okawachi, M. R. Lamont, A. L. Gaeta, M. Lipson, Broadband mid-infrared frequency comb generation in a Si_3N_4 microresonator, Optics Letters 40 (21) (2015) 4823–4826.

[41] T. Bååk, Silicon oxynitride; a material for grin optics, Applied Optics 21 (6) (1982) 1069–1072.

[42] K. Mohsin, M. S. Alam, D. M. N. Hasan, M. N. Hossain, Dispersion and nonlinearity properties of a chalcogenide As_2Se_3 suspended core fiber, Applied Optics 50 (25) (2011) E102–E107.

[43] M. J. Dodge, Refractive properties of magnesium fluoride, Applied Optics 23 (12) (1984) 1980–1985.

[44] K. Mo, B. Zhai, L. Jianfeng, E. Coscelli, F. Poli, A. Cucinotta, S. Selleri, C. Wei, Y. Liu, Numerical investigation on broadband mid-infrared supercontinuum generation in chalcogenide suspended-core fibers, Chinese Physics B 26 (5) (2017) 054216.

[45] D. Duchesne, M. Peccianti, M. R. Lamont, M. Ferrera, L. Razzari, F. Légaré, R. Morandotti, S. Chu, B. E. Little, D. J. Moss, Supercontinuum generation in a high index doped silica glass spiral waveguide, Optics Express 18 (2) (2010) 923–930.

[46] G. P. Agrawal, Nonlinear fiber optics, 5th ed., Academic Press, 2013.

[47] C. Flueraru, C. P. Grover, Overlap integral analysis for second-harmonic generation within inverted waveguide using mode dispersion phase match, IEEE Photonics Technology Letters 15 (5) (2003) 697–699.

[48] H. Hu, W. Li, X. Zhang, N. K. Dutta, Broadband supercontinuum generation in a tapered-rib lead-silicate waveguide, International Journal of High Speed Electronics and Systems 24 (03n04) (2015) 1550009.

[49] H. Ahmad, M. R. Karim, B. Rahman, Modeling of dispersion engineered chalcogenide rib waveguide for ultraflat mid-infrared supercontinuum generation in all-normal dispersion regime, Applied Physics B 124 (3) (2018) 47.

[50] J. M. Dudley, S. Coen, Numerical simulations and coherence properties of supercontinuum generation in photonic crystal and tapered optical fibers, IEEE Journal of Selected Topics in Quantum Electronics 8 (3) (2002) 651–659.

[51] X. Gu, M. Kimmel, A. P. Shreenath, R. Trebino, J. M. Dudley, S. Coen, R. S. Windeler, Experimental studies of the coherence of microstructure-fiber supercontinuum, Optics Express 11 (21) (2003) 2697–2703.